A simple method for estimating transition locations on blade surface of model propellers to be used for calculating viscous force

Huilan Yao [a,b], Huaixin Zhang [a,b,*]

[a] *State Key Laboratory of Ocean Engineering, School of Naval Architecture, Ocean and Civil Engineering, Shanghai Jiao Tong University, Shanghai 200240, China*
[b] *Collaborative Innovation Center for Advanced Ship and Deep-Sea Exploration (CISSE), Shanghai 200240, China*

Abstract

Effects of inflow Reynolds number (Re), turbulence intensity (I) and pressure gradient on the transition flow over a blade section were studied using the γ-$Re\theta$ transition model (STAR-CCM+). Results show that the Re_T (transition Re) at the transition location (P_T) varies strongly with Re, I and the magnitude of pressure gradient. The Re_T increases significantly with the increase of the magnitude of favorable pressure gradient. It demonstrates that the Re_T on different blade sections of a rotating propeller are different. More importantly, when there is strong adverse pressure gradient, the P_T is always close to the minimum pressure point. Based on these conclusions, the P_T on model propeller blade surface can be estimated. Numerical investigations of pressure distribution and transition flow on a propeller blade section prove these findings. Last, a simple method was proposed to estimate the P_T only based on the propeller geometry and the advance coefficient.
Copyright © 2017 Society of Naval Architects of Korea. Production and hosting by Elsevier B.V. This is an open access article under the CC BY-NC-ND license (http://creativecommons.org/licenses/by-nc-nd/4.0/).

Keywords: Transition flow; Viscous force; Strip method; Propeller performance

1. Introduction

So far, the performance prediction of propulsion systems is mainly based on the results of open water tests in model scale. Due to the limitation of experimental conditions, model propellers cannot be as large as the full scale propeller, and the rotation rate is also limited. The Reynolds number (Re) of model propellers (based on $0.75R$ blade section, where R is the radius of the propeller) is much smaller than that of the full scale propellers, which makes the boundary layer flow of the model propeller very different from that of the full scale propeller. The different boundary layer flows make different viscous forces and different propulsion performances, known as scale effects. To obtain accurate performance of the full

scale propeller, the measured data of the model propeller need to be scaled.

The study of propeller scale effects has been carried out for decades. The key is to accurately predict the viscous force of the model propeller with complex boundary layer flows because of the low Re. There are several scaling methods to scale the measured model propeller data to full scale propeller performance, and four of them are frequently used today: no scaling, the Lerbs−Meyne method (Meyne, 1968), the 1978 ITTC scaling method (ITTC, 1978) and the strip method (Praefke, 1994; Streckwall et al., 2013). A brief introduction about the four scaling methods is available in Helma (2015). In the strip method, the vector sum of contributions of each radial section (strip) towards the friction resistance is calculated to get the friction resistance of the whole blade. Theoretically, the strip method is a relatively accurate approach of the existing scaling methods (the 1978 ITTC scaling method is only based on the friction of one blade section). However, the calculation of the viscous force needs the transition location

---

* Corresponding author.
   E-mail address: huaixinzhang@126.com (H. Zhang).
   Peer review under responsibility of Society of Naval Architects of Korea.

Nomenclature

C and $C_{0.75R}$ chord length of the airfoil and the $0.75R$ propeller blade section

C_f local friction coefficient

C_p local pressure coefficient

C_T length from the leading edge to the transition point P_T

D diameter of the propeller

I turbulence intensity $= \sqrt{(2/3)k}/\bar{v}$

J advance coefficient

k turbulent kinetic energy

K_T propeller thrust coefficient

K_Q propeller torque coefficient

L length of the flat plate

n rotational rate of the propeller

P pitch of a blade section

P_T transition location, where the flow changes from laminar to turbulent region

R radius of the propeller

r radius of a blade section, $r = \eta R$, η is between 0 and 1

Re inflow Reynolds number to the flat plate and the propeller

$Re_{0.75R}$ inflow Reynolds number to the $0.75R$ propeller blade section

Re_T local Reynolds number at the transition location P_T

T turbulent time scale

u_a and u_t induced axial velocity and circumferential velocity by the propeller

Z blade number

$\bar{v}$ the mean reference velocity

V_A advance velocity for the propeller

V_x and V_θ axial velocity and tangential velocity in propeller's wake

V_n relative circumferential velocity $= 2\pi nr$

V_R resultant velocity of u_a, u_t, V_A and V_n

α_K and α'_K angle of attack and approximated angle of attack

θ pitch angle

β advance angle

β_i hydrodynamic pitch angle

ρ density of water

μ_t turbulent viscosity

μ natural molecular viscosity of water

ν kinematic viscosity

ε and ω turbulent dissipation rate in turbulence models

γ intermittency, for trigging the transition

$Re\theta$ momentum thickness Reynolds number

$\varepsilon(K_T)$ and $\varepsilon(10K_Q)$ $\varepsilon(K_T) = (K_{T,Fine} - K_{T, Middle})/K_{T, Middle}$, $\varepsilon(10K_Q) = (10K_{Q,Fine} - 10K_{Q, Middle})/10K_{Q, Middle}$

$\lambda(K_T)$ and $\lambda(10K_Q)$ $\lambda(K_T) = (K_{T,Num} - K_{T, Exp})/K_{T, Exp}$, $\lambda(10K_Q) = (10K_{Q,Num} - 10K_{Q, Exp})/10K_{Q, Exp}$

M-P-G magnitude of pressure gradient $= \Delta C_p/\Delta x$

ΔC_p the difference of local pressure coefficients of two adjacent cells

Δx the distance between two adjacent cells

TVR turbulence viscosity ratio $= \mu_t/\mu$

A-P-G   adverse pressure gradient

F-P-G   favorable pressure gradient

Exp   experimental data

Num   numerical results

SST   shear stress transport

SST-kε   a turbulence model; applying the kε model in the far-field for high speed flow region and the kω model near the wall for low speed flow region

Realizable kε   a turbulence model; based on the standard kε model; suitable for boundary layer flow simulation

γ-Reθ   a transition model; based on the SST-kω model; two additional transport equations need to be solved for predicting transition

(P_T) on each radial section of the whole blade surface. Since the boundary layer transition flow on the blade surface is very complex because of too many factors affecting the transition, the transition locations on all sections of the whole blade calculated only based on two assumed transition Reynolds numbers (Re_T) (one for the blade face and the other for the blade back) remains questionable, even though two other assumed Re_T were applied considering the effect of turbulence intensity (Streckwall et al., 2013).

Recently, with the development of the γ-Reθ transition model within the RANS code (Menter et al., 2006), the numerical study of the transition flow of model propellers was beginning to emerge in the past few years. In 2010, Müller et al. (2009) and Müller (2013) applied the transition model for studying the transition flow of a model propeller. In 2014, Sánchez-Caja et al. (2014) studied the scale effects on tip loaded propeller performance. In 2016, Bhattacharyya et al. (2015, 2016a, 2016b) used the transition model for studying the transition flow of a ducted propeller, and a scaling approach was proposed by way of regression. Generally, the γ-Reθ transition model gives us a powerful tool for a deep insight to the transition flow on the model propeller blade surface.

In this paper, the γ-Reθ transition model was applied for studying the transition flow of a model propeller, especially the transition Reynolds number (Re_T) and the P_T on the blade surface. The primary work was introduced as follows. First, the accuracy of the transition model was validated by simulating the transition flow of a flat plate and a two-dimensional airfoil. Numerical results were compared with available experimental data. Second, to simplify the research, the transition flow of a marine propeller was studied first by simulating that on a propeller blade section. The effects of Re, I (turbulence intensity) and the magnitude of pressure gradient on the transition flow were studied. Major conclusions about

estimating the transition locations on the blade section were made. Third, the transition model was applied for simulating the transition flow of a model propeller in open water, and different working conditions were simulated. Grid independence verification and validation were performed based on available experimental data. Fourth, numerical results of pressure distribution, transition flow and friction distribution on the propeller blade section ($0.75R$) were studied. More importantly, the relationship between the pressure gradient and the transition location was studied. In the end, a simple method was proposed to estimate the transition location on the model propeller blade surface.

2. Two cases for validating the transition model

2.1. Transition flow with zero pressure gradient

The γ-Reθ transition model was validated by simulating the transition flow on a smooth flat plate with zero pressure gradient. The data used for validation are the skin friction data of Schubauer and Klebanoff (1955). The computational mesh is shown schematically in Fig. 1. A specified constant velocity inlet (50.1 m/s) was used together with the turbulent kinetic energy (k) and dissipation rate (ω) as 0.0827 J/kg and 5134 s^{-1}, respectively. The mesh contains 325 stream-wise and 200 cross-stream quad cells, with a near-wall cell height of $1.0 \cdot 10^{-6}$ m. The mesh is even finer than that in Malan et al. (2009), where mesh sensitivity studies of the domain extent, the wall-adjacent cell height and the cell count were made to ensure a mesh-independent result. Fig. 2(a) shows the decay rate of I in the free-stream. Here and after, the equation for obtaining I is defined as $I = \sqrt{2/3k}/\overline{v}$, where k is the turbulent kinetic energy, $\overline{v}$ is the mean reference velocity. From Fig. 2(a), the decrease of I in the free stream is obvious, and the decay rate is in line with Malan et al. (2009) (no experimental data are available). Fig. 2(b) shows the friction distribution predicted by the γ-Reθ transition model and two turbulence models (SST-kω and Realizable kε) (Cd-Adapco, 2015). The agreement between the predictions by the transition model and the experimental data is very good. It is also clear that the friction distributions on the plate calculated by the two turbulence models are inaccurate because the transition was not predicted.

The realizable kε model is based on the standard kε model (for high Reynolds numbers problems) using a new transport

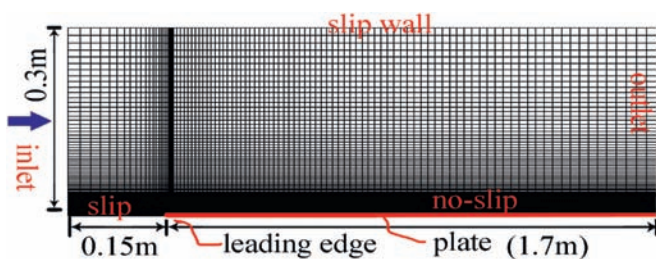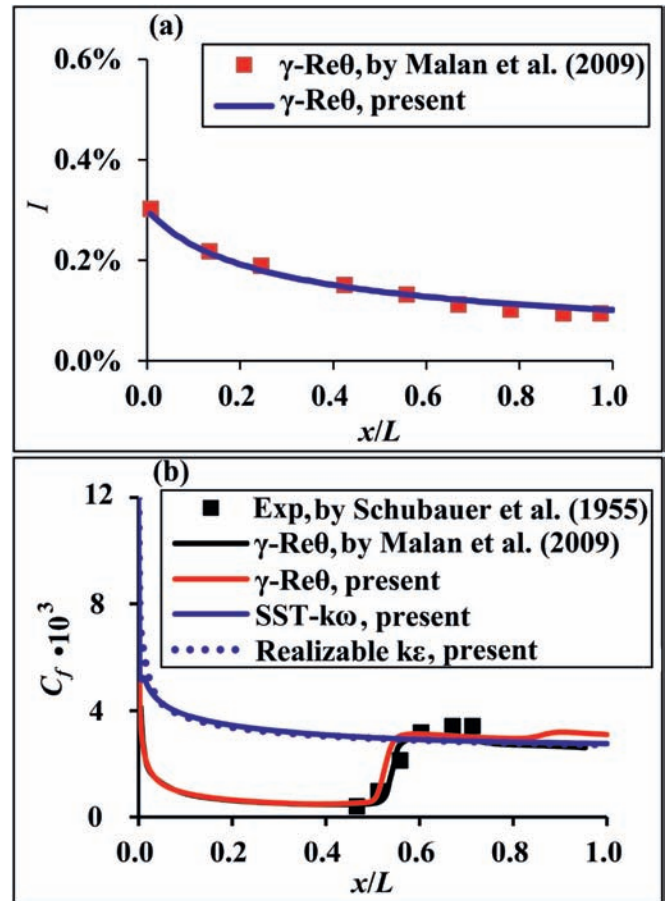Fig. 2. Turbulence decay rate in the free-stream (a) and the friction distribution on the smooth flat plate (b).

equation for the turbulent dissipation rate (ε), and this model is suitable for boundary layer flow simulation. The SST-kω model is based on the standard kω model (considering low Reynolds number problems, especially the low velocity flow near the wall). In this model, the kε model is applied in the far-field for the high velocity flow region and the kω model is applied in the boundary layer. The γ-Reθ transition model is only based on the SST-kω model and solves two additional transport equations for predicting the transition phenomenon.

2.2. Transition flow with non-zero pressure gradient

The γ-Reθ transition model was also validated by simulating the transition flow of a two-dimensional airfoil (Chaput, 1997). The ONERA F2 wind tunnel data (the angle of attack is 13.3° and the inflow Reynolds number is $2.1 \cdot 10^6$) are used for this validation. The geometry of the airfoil, computational domain and boundary layer meshes of the airfoil are presented in Fig. 3. The near-wall mesh spacing is $1.0 \cdot 10^{-5}$ chord lengths, resulting in a peak value of wall Y$^+$ under 0.8. The mesh is fine enough to yield a mesh-independent result (Malan et al., 2009). The F2 wind tunnel has a very low level of turbulence in the test section (less than 0.05%). In our study, the turbulence intensity at the inlet boundary was set to 0.02%. Fig. 4 shows a comparison of numerical results with the

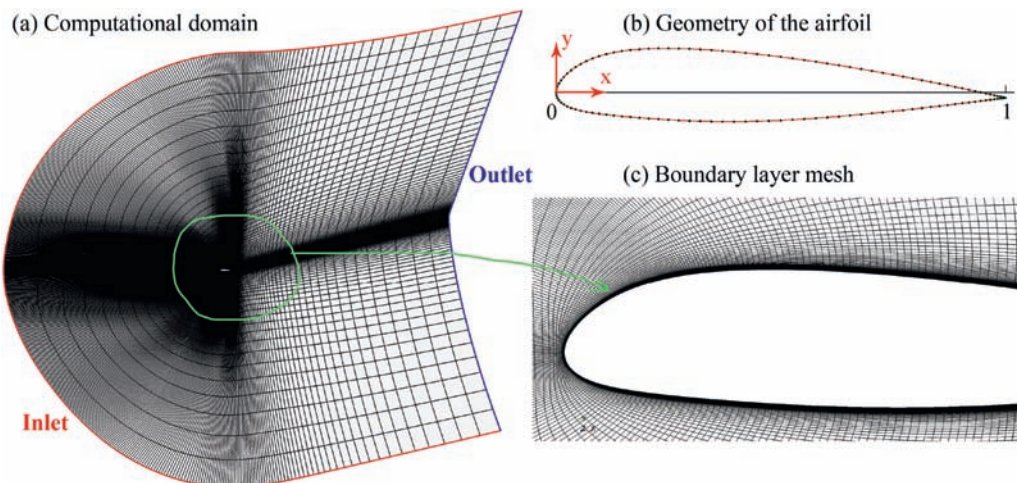Fig. 1. Mesh schematic for the simulation of transition flow over a smooth flat plate.

Fig. 3. Mesh schematic for the simulation of transition flow over a two-dimensional airfoil.

experimental data (Exp. data). Generally, the pressure distribution predicted by the transition model agrees well with the experimental data. There is a long region of favorable pressure gradient (F-P-G) on the pressure side, and a long region of adverse pressure gradient (A-P-G) on the suction side (Fig. 4(a)). Numerical results of viscous effects on the suction side are close to the experimental data, and the transition location (P_T) was accurately predicted (Fig. 4(b)).

3. Effects of Reynolds number, turbulence intensity and pressure gradient on the transition flow

Each blade section of marine propellers is similar to a two-dimensional airfoil. To simplify the research and save computer resources, the effects of three key factors on the transition flow over model propeller blades were studied by simulating the transition flow of a blade section. The geometry of the airfoil in Section 2.2 was used. Computational domain, meshes and numerical methods are exactly the same as that introduced in Section 2.2.

3.1. Reynolds number

As known, marine propellers are designed to produce thrust to push the ship forward. Therefore, there is a certain positive angle of attack between the inflow and the blade section. For a blade section with a positive angle of attack, the pressure gradient on the blade section is inevitable. The effects of Reynolds number and pressure gradient on the transition were studied together. In this Section, the angle of attack was set to 12°. Different Reynolds numbers are achieved by changing the inflow velocity using the following equation: $Re = VC/\nu$, where V is the inflow velocity, C is the chord length of the blade section and ν is the kinematic viscosity of water. Ten cases (Table 1) were selected for the study. These Reynolds numbers are chosen considering the following conditions: the Reynolds number of the model propeller in experiments is in
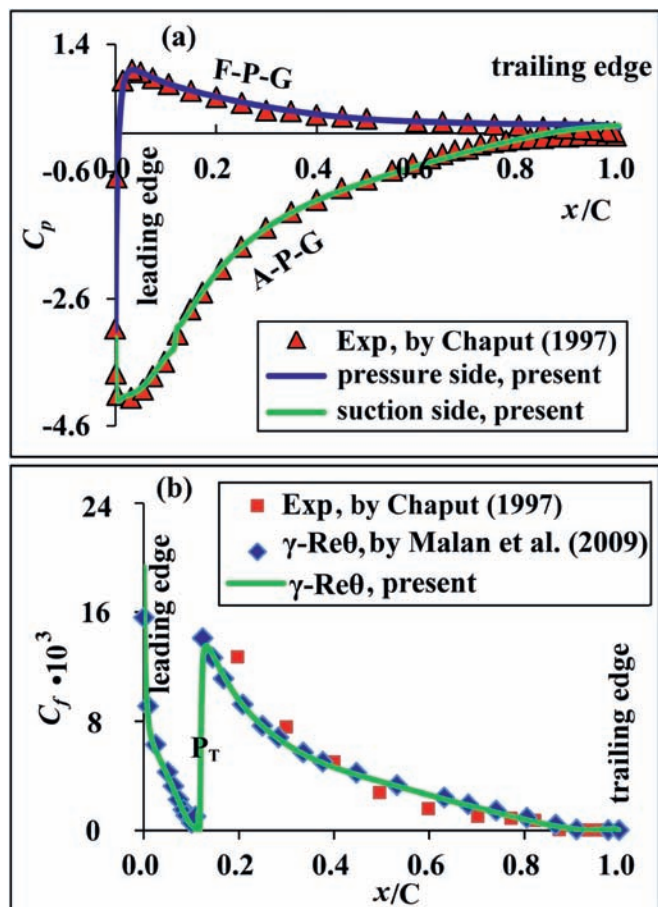

Fig. 4. The pressure distribution on the airfoil (a) and the friction distribution on the suction side (b), $Re = 2.1 \cdot 10^6$.

Table 1
Ten cases for studying the effect of Reynolds number on the transition flow over a blade section.

V	0.1 m/s	0.2 m/s	0.4 m/s	0.7 m/s	1.0 m/s
Re	$2.1 \cdot 10^5$	$2.3 \cdot 10^5$	$4.5 \cdot 10^5$	$7.9 \cdot 10^5$	$1.1 \cdot 10^6$
V	2 m/s	4 m/s	6 m/s	8 m/s	10 m/s
Re	$2.3 \cdot 10^6$	$4.5 \cdot 10^6$	$6.8 \cdot 10^6$	$9.0 \cdot 10^6$	$1.1 \cdot 10^7$

the order of magnitude of 10^5, and that of the full scale propeller is in the order of magnitude of 10^7.

Fig. 5(a) shows the pressure gradient on the blade section when the angle of attack is 12°, and the pressure gradient on the blade section with different Re is basically the same (they are not presented in Fig. 5(a)). On the pressure side, there is a long region of F-P-G. On the suction side, there is a long region of strong A-P-G after the minimum pressure point. Fig. 5(b) and (c) shows the transition point (P_T) and the transition Reynolds number (Re_T) on the pressure side at different Re. It is clear that the position of P_T and the Re_T on the pressure side varies strongly with Re. Fig. 5(d) and (e) shows the P_T and the Re_T on the suction side at different Re. The Re_T on the suction side still varies a lot with Re. However, a strange phenomenon was found in Fig. 5(d), where the positions of all P_T on the suction side at different Re seem to be very close. Referring to Fig. 5(a), all P_T on the suction side are located in the A-P-G region and close to the minimum pressure point, and the greater the Reynolds number, the closer the

P_T to the minimum pressure point. Comparing Fig. 5(b) with (d), for the pressure side and the suction side at the same Re, the development of laminar flow on the suction side is greatly hindered. The possible reason is the strong A-P-G on the suction side.

Fig. 6 shows the relationship between the Re_T and the inflow Reynolds number. It is clear that the Re_T is a function of the inflow Reynolds number. Considering that the Re to the blade section of a rotating propeller varies strongly along the radial direction, the transition flow on the whole propeller blades estimated by two assumed Re_T remains questionable. From Fig. 6, under the effects of F-P-G or A-P-G, both Re_T on the pressure side and suction side increases with the increase of Re, but the increase of Re_T on the pressure side is much more pronounced than that on the suction side. It means that the pressure side is covered by much more laminar flow than the suction side at the same inflow Reynolds number. Based on this conclusion, it can be inferred that the laminar area on the blade face of the model propeller is larger than that on the blade back.
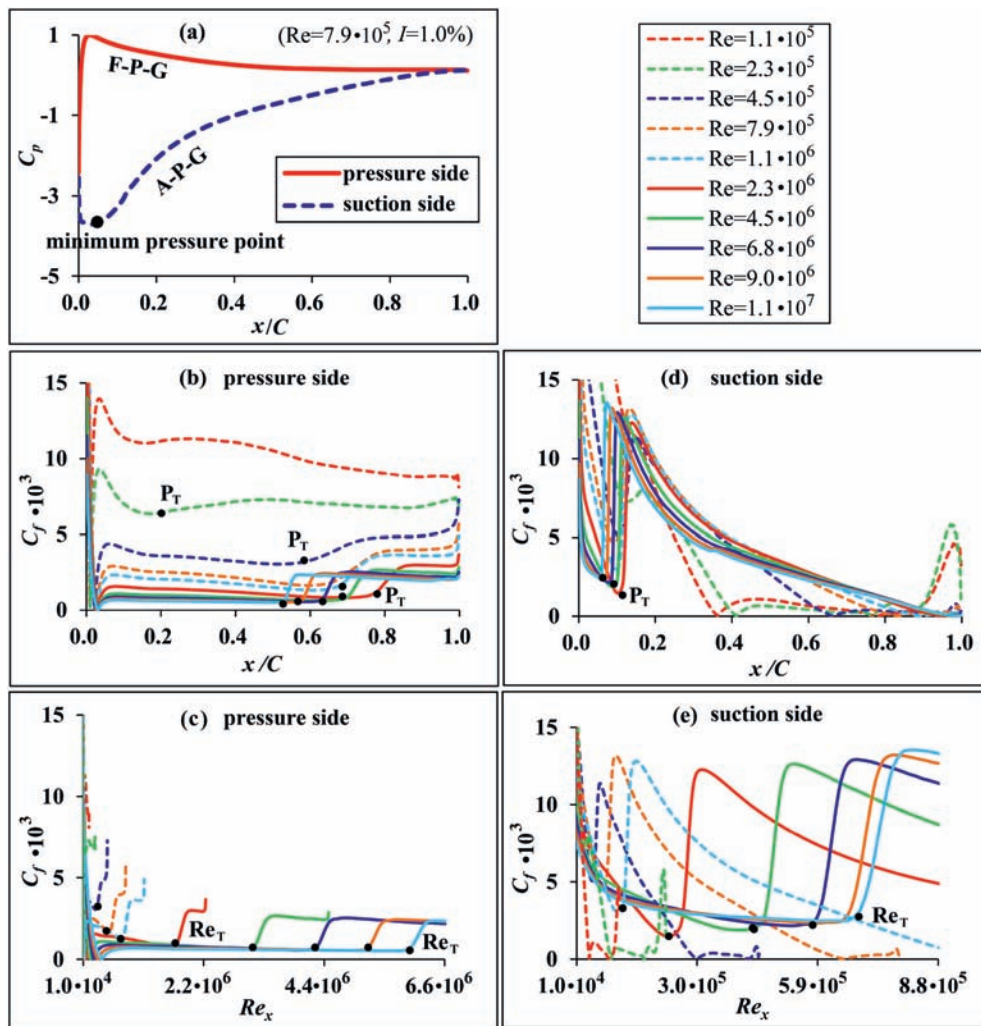

Fig. 5. Re_T and P_T on the blade section at different Reynolds numbers when the angle of attack is 12°, $Re = 7.9 \cdot 10^5$, $I = 1.0\%$: (a) pressure gradient on the blade section, (b) P_T on the pressure side, (c) Re_T on the pressure side, (d) P_T on the suction side, (e) Re_T on the suction side.
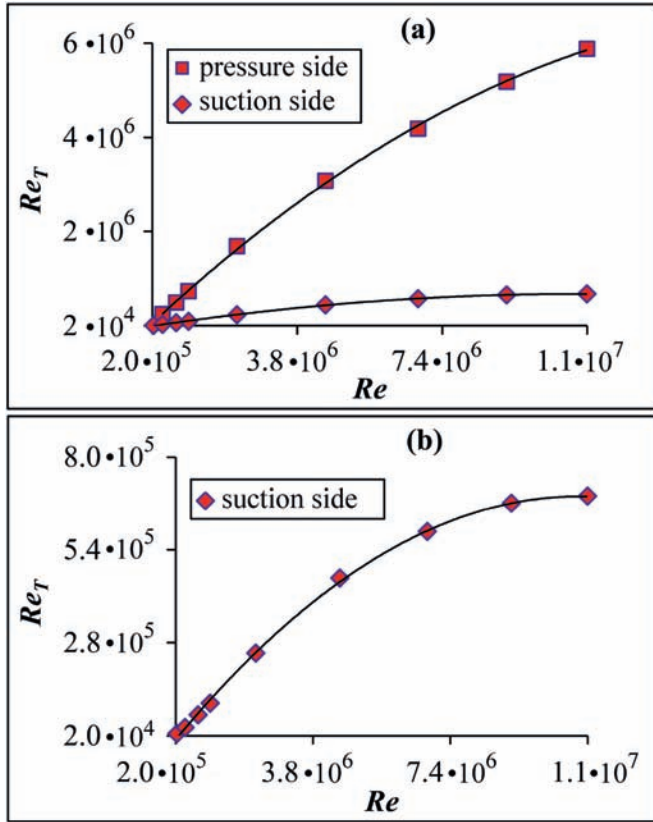
Fig. 6. Relationship between the Re_T and the inflow Reynolds number (a) and a detailed view of the relationship curve on the suction side (b), $I = 1.0\%$.

3.2. Turbulence intensity

In this study, the inflow velocity is kept the same, and the angle of attack is set to $12°$. Different values of I are set to the velocity inlet boundary. To maintain the turbulence intensity to the leading edge of the blade section because of the turbulence decay along the free-stream, the ambient function (Cd-Adapco, 2015) is turned on, which adds a source term to the transport equations to counteract turbulence decay in external flows. Fig. 7 shows a comparison of the turbulence decay in the free-stream when the ambient function is turned on or not.
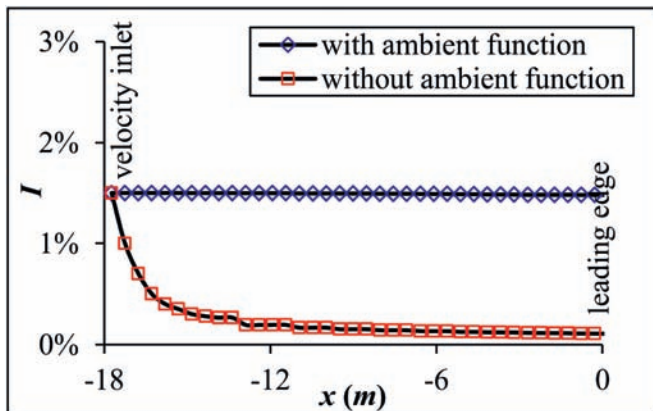

Fig. 7. A comparison of the turbulence decay in the free-stream when the ambient function is turned on or not, $V = 10$ m/s, $Re = 1.1 \cdot 10^7$.

It is clear that the turbulence intensity set at the inlet boundary maintained to the leading edge when the ambient function is turned on. Fig. 8 shows the viscous effects on the pressure side and the suction side. First, the pressure distribution on the blade section is similar to that shown in Fig. 5(a). From Fig. 8, although the Reynolds number keeps the same, the transition location on the pressure side still varies strongly with I. However, the laminar flow region on the suction side at different I values is basically the same. The transition locations are very close and near to the minimum pressure point. It suggests that the effect of I on the transition is greatly reduced by the strong A-P-G on the suction side.

3.3. Pressure gradient

In this section, the effect of the magnitude of pressure gradient (M-P-G) on the transition location was investigated (M-P-G $= \Delta C_p / \Delta x$), where ΔC_p and Δx are calculated using the values of two adjacent cells, as shown schematically in Fig. 9(a). The change of M-P-G was achieved by changing the angle of attack. Fig. 9(a−c) shows the effect of the magnitude of F-P-G on the transition flow over the pressure side. From Fig. 9(a), the magnitude of F-P-G on the pressure side increases with the increase of angle of attack. From Fig. 9(b), the Re_T increases significantly with the increase of the
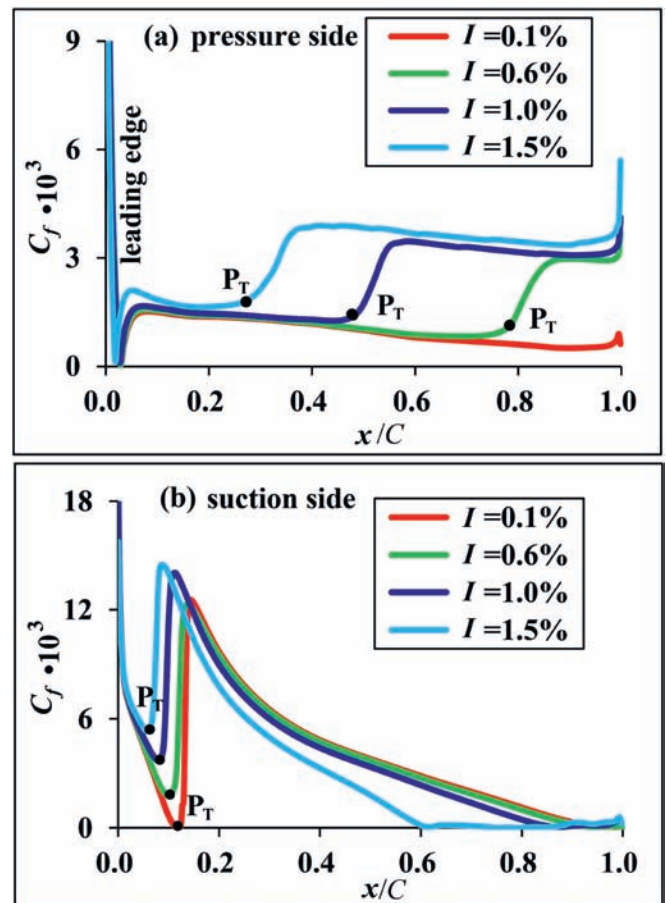

Fig. 8. Effects of turbulence intensity on the transition location over the pressure side (a) and the suction side (b), $Re = 1.1 \cdot 10^7$.
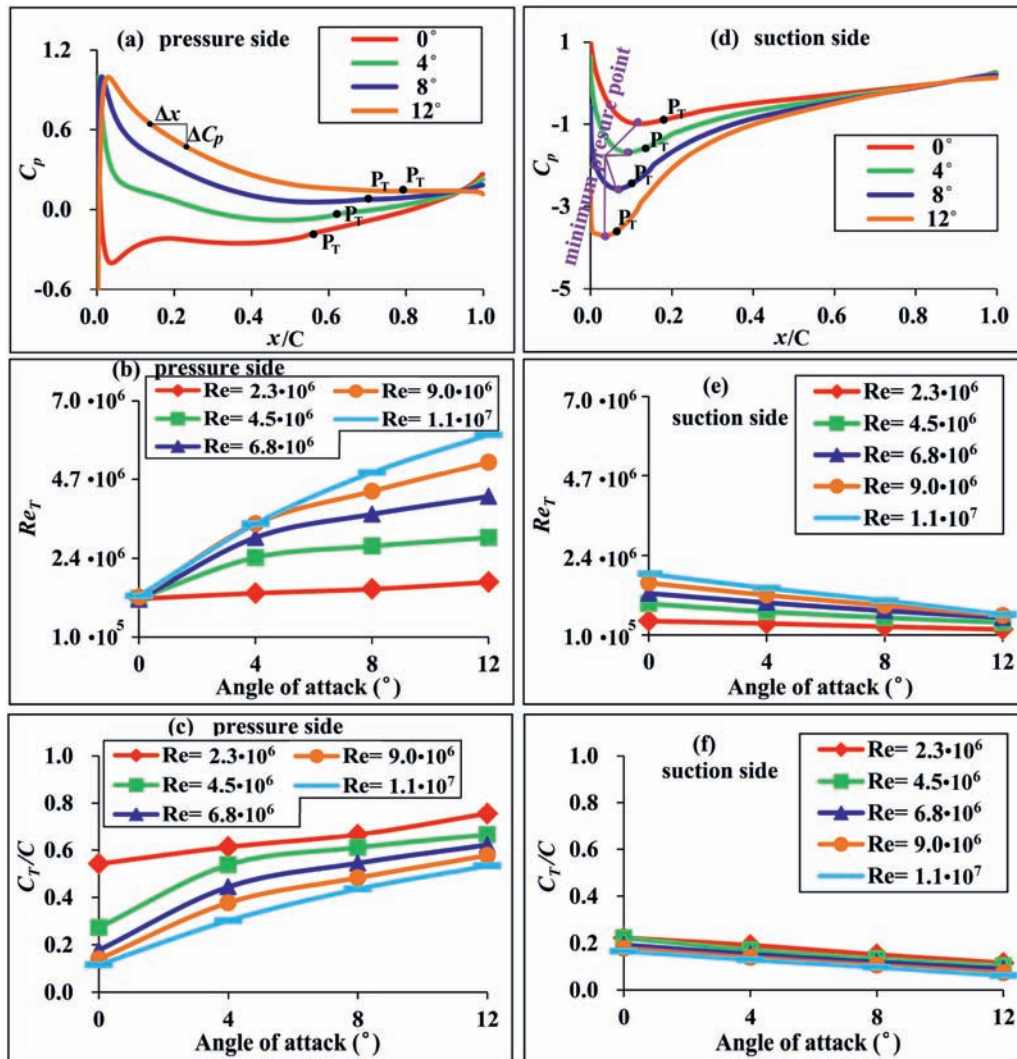
Fig. 9. Effects of the magnitude of pressure gradient on the transition over a blade section, $I = 1.0\%$: (a) F-P-G on the pressure side, $Re = 4.5 \cdot 10^6$, (b) Re_T on the pressure side, (c) C_T/C on the pressure side, (d) A-P-G on the suction side, $Re = 4.5 \cdot 10^6$, (e) Re_T on the suction side, (f) C_T/C on the suction side.

magnitude of F-P-G. From Fig. 9(c), the area of laminar flow increases with the increase of the magnitude of F-P-G (here, C_T is the distance between the leading edge and P_T). Fig. 9(d−f) shows the effect of the magnitude of A-P-G on the transition flow over the suction side. From Fig. 9(d), the magnitude of A-P-G increases with the increase of attack angle. From Fig. 9(e), the Re_T decreases with the increase of the magnitude of A-P-G. From Fig. 9(f), the transition locations on the suction side with different magnitudes of A-P-G are very close. The transition location is getting closer to the minimum pressure point with the increase of the magnitude of A-P-G.

3.4. Discussions

Fig. 10 shows the pressure distribution on the blade section of a marine propeller in the most general case, which is similar to that shown in Fig. 5(a). On the suction side, there is a long region of strong A-P-G, and a long region of strong F-P-G exists on the pressure side. Based on the conclusions from

Section 3, the transition point of the flow on the suction side is located in the A-P-G region and close to the minimum pressure point. However, the determination of the transition point on the pressure side is more complicated (Reynolds number dependent), but one thing that can be sure is that the laminar flow area on the pressure side is much larger than that on the suction side, and the greater the magnitude of the F-P-G on the pressure side is, the larger the area of the laminar flow will be. Generally, all these conclusions can be extended to each blade section of the whole propeller.

4. Marine propeller simulations

4.1. Propeller geometry

According to the recommendation of the 27th ITTC (ITTC, 2014), the model propeller VP1304 was selected for the study. Barkmann (2011) performed the open-water test in the towing tank, and Mach (2011) measured the velocities in the cavitation tunnel. The measurements were made public and can be
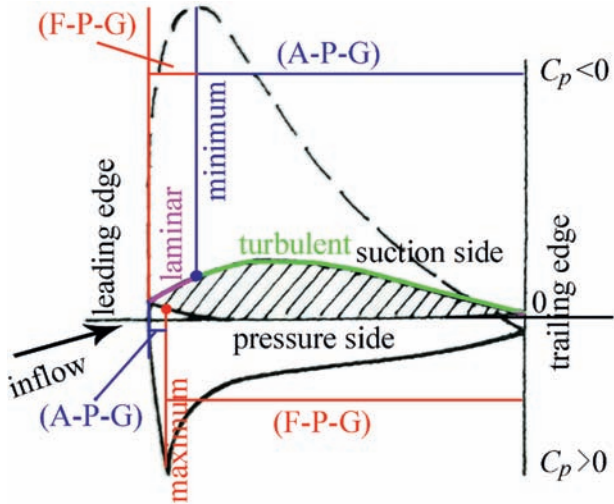
Fig. 10. Sketches of determining the transition flow based on the pressure distributions on the blade section of propellers in the most general case.

used for validating numerical studies. Geometry and primary parameters of the propeller are presented in Fig. 11. Table 2 lists the Reynolds numbers of the model propeller in model tests.

4.2. Numerical setup

The computational domain for propeller simulations is shown in Fig. 12, where D is the diameter of the propeller. There is a small rotating domain wrapping the whole propeller, and the rest of the domain is set to be stationary. On the velocity inlet boundary, inflow velocity was specified based on the equation $V_A = JnD$. On the pressure outlet boundary, the static pressure was set to zero. Moving reference frame and rigid motion model were used in the rotating domain for simulating the motion of propellers. A steady simulation was performed first for 2000 steps to obtain an initial flow fields around the propeller for the unsteady simulations. Time scale of the unsteady simulation was set to the time of the propeller rotating one degree, and each time step iterates ten times.

The entire domain is discretized using the Trimmed Cell Mesher (Cd-Adapco, 2015). Local mesh schematic near the rotating propeller was presented in Fig. 13. The strips on the

Fig. 11. Geometry and primary parameters of the model propeller VP1304.

Table 2
Reynolds numbers of the model propeller VP 1304 at different advance coefficients.

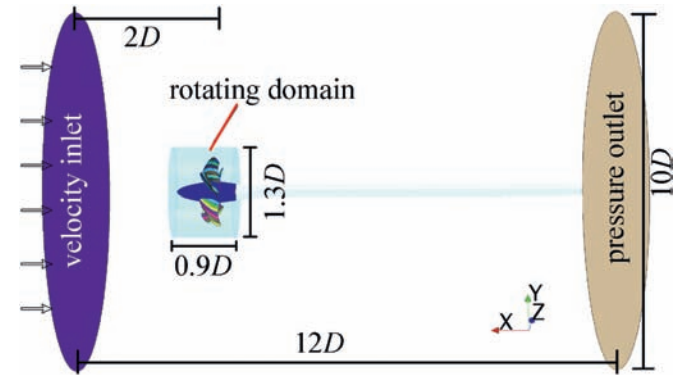|	$J = 0.2$	$J = 0.6$	$J = 0.8$	$J = 1.0$	$J = 1.2$	$J = 1.4$
$Re_{0.75R}$	$8.3 \cdot 10^5$	$8.5 \cdot 10^5$	$8.7 \cdot 10^5$	$9.0 \cdot 10^5$	$9.3 \cdot 10^5$	$9.6 \cdot 10^5$

Fig. 12. Computational domain and main boundary conditions for propeller simulations.
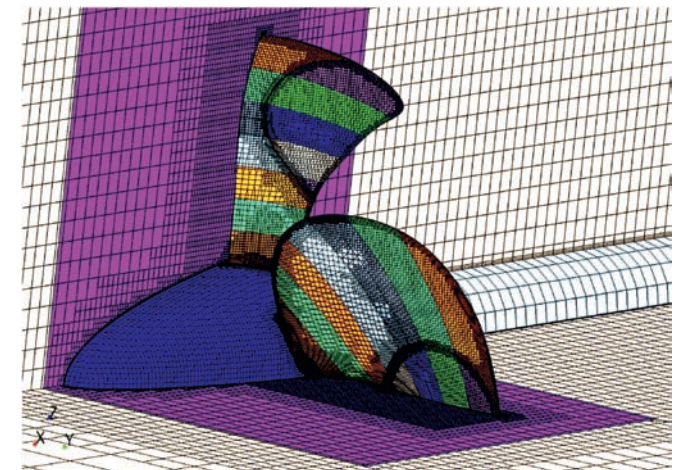

Fig. 13. Local mesh schematic for numerical simulations of propeller VP1304.

blade surface were purposely designed. As known, local Re of each blade section changes strongly along the radial direction from the blade root to the tip for a rotating propeller. To keep the wall Y^+ values on the whole blade surface within the optimal range as required, the height of the first layer of the grid at different radii should be different and needs to be specified respectively. The low Y^+ wall treatment is used to resolve the near-wall turbulence effects and predicting accurate skin friction. Twenty layers of elements within the boundary layer are generated, as presented in Fig. 14. Predicted wall Y^+ distribution on the blade back shows that all values are basically less than 1.

Since no information about the turbulence intensity has been found in the published experimental reports, in this paper, each case with two different I values (0.5% and 5%) set at the velocity inlet boundary were simulated to study the effect of I on the transition.
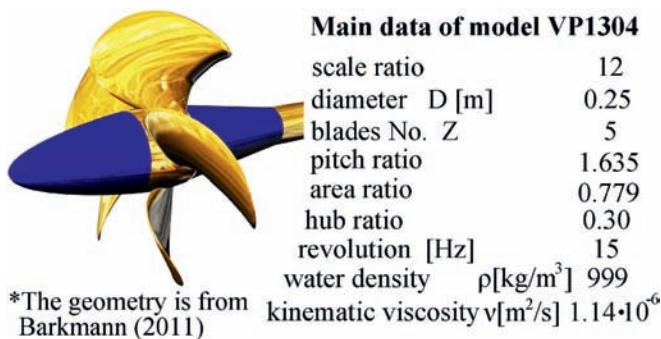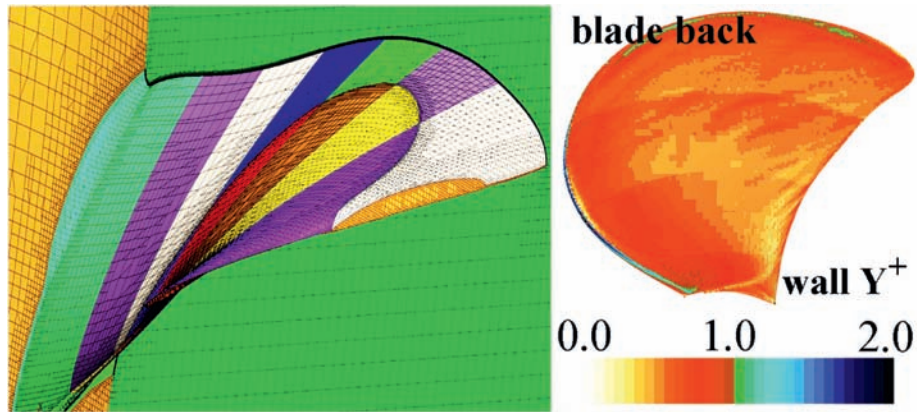
Fig. 14. Boundary layer meshes and wall Y+ distributions on the blade back of propeller VP1304 ($J = 0.8$).

4.3. Grid independence verification and validation

Velocity measurements (Mach, 2011) of the model propeller at a loading condition ($J = 1.253$, $n = 23$ Hz, $V_A = 7.204$ m/s, $Re = 1.43 \cdot 10^6$, $I = 0.5\%$, $K_T = 0.250$, $10K_Q = 0.725$) were used for the grid independence verification and validation study. Three cases with different mesh resolutions were simulated. Numerical results of K_T and $10K_Q$ were presented in Table 3, where two scalars are defined: $\varepsilon(K_T) = (K_{T,\text{Fine}} - K_{T,\text{Middle}})/K_{T,\text{Middle}}$ for the grid independence verification and $\lambda(K_T) = (K_{T,\text{Num}} - K_{T,\text{Exp}})/K_{T,\text{Exp}}$ for the validation; the equations for $10K_Q$ are similar to that for K_T. It is clear that these two coefficients ($\varepsilon(K_T)$ and $\varepsilon(10K_Q)$) change very little (less than 1.24%) when the total cell number increases from 3.68 million to 5.21 million cells. It means that the numerical results are minimally influenced by the mesh resolution when the cell number reaches 5.21 million. As for the validation, the differences between the numerical predictions (the case with 5.21 million cells) and the measured data are less than 2.0%. It suggests that the numerical methods are credible. Circumferential distributions of axial and tangential velocity of 0.7R profile of a section 0.1D downstream of the propeller plane were compared with the measurements (Mach, 2011) in Fig. 15. Generally, the velocity distributions predicted by the three cases with different mesh resolutions agree well with each other as well as the measured results. When looking closer, the fine case provides the closest results to the measured results. From the grid independence study, the case with 5.21 million cells was chosen for the following study.

4.4. Open water performance

The transition model with two different I and two turbulence models (SST-kω and the Realizable kε) were applied for propeller simulations in open water. Four working conditions were simulated using the fine mesh case: a heavy loading ($J = 0.2$), two moderate loadings ($J = 0.6$ and $J = 0.8$), and a light loading ($J = 1.4$). The rotational rate (n) was set to 15 Hz. Reynolds numbers are between $8.3 \cdot 10^5$ and $9.6 \cdot 10^5$. Numerical results of K_T and $10K_Q$ (by the transition model) are presented in Table 4. The prediction error between the numerical results and the experimental data (Barkmann, 2011) is shown in Fig. 16. The prediction error is calculated by the following expression: (numerical results − experimental data)/experimental data × 100%. Generally, numerical results predicted by the transition model
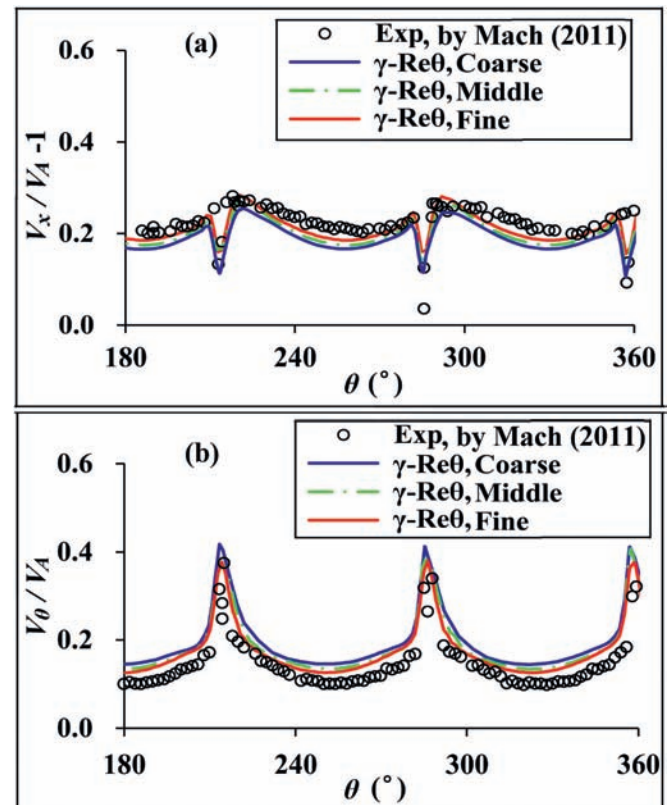

Fig. 15. Circumferential distributions of axial velocity (a) and tangential velocity (b) of 0.7R profile of a section 0.1D downstream of the propeller plane using three mesh cases, $J = 1.253$, $Re = 1.43 \cdot 10^6$, $I = 0.5\%$.

Table 3
Grid independence verification and validation for numerical simulations of the model propeller VP1304 in open water.

Cases	Number of cells	K_T	$10K_Q$	$\varepsilon(K_T)$	$\varepsilon(10K_Q)$	$\lambda(K_T)$	$\lambda(10K_Q)$
Coarse	2.70 million	0.231	0.692	/	/	−7.6%	−4.6%
Middle	3.68 million	0.242	0.705	4.76%	1.9%	−3.2%	−2.8%
Fine	5.21 million	0.245	0.713	1.24%	1.1%	−2.0%	−1.7%

Table 4
Open water performance of the propeller VP1304 predicted by the transition model with two different I values and the experimental data (Barkmann, 2011).

	K_T			$10K_Q$		
	γ-Re$\theta_{(I = 0.5\%)}$	γ-Re$\theta_{(I = 5\%)}$	Exp	γ-Re$\theta_{(I = 0.5\%)}$	γ-Re$\theta_{(I = 5\%)}$	Exp
$J = 0.2$	0.8823	0.8832	0.8663	1.9210	1.9228	1.8638
$J = 0.6$	0.6286	0.6257	0.6288	1.4107	1.4044	1.3964
$J = 0.8$	0.5107	0.5082	0.5100	1.1931	1.1887	1.1780
$J = 1.4$	0.1785	0.1684	0.1878	0.5404	0.5160	0.5588
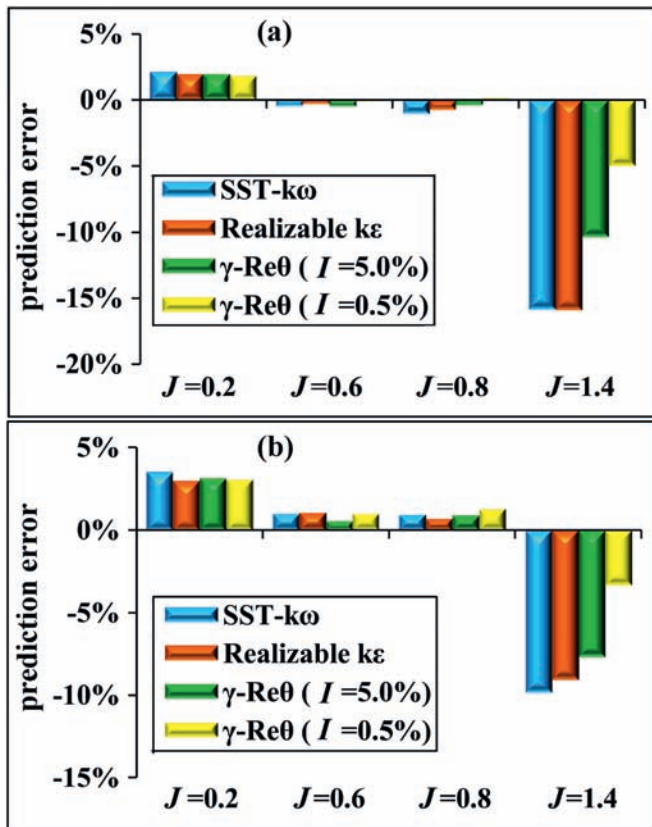
Fig. 16. Prediction error between the numerical results (the transition model with two different I and two turbulence models) of K_T (a) and $10K_Q$ (b) and the experimental data.

are better than that by the turbulence model, especially in high J. However, the advantage of the transition model in heavy and moderate loadings is small. This is because the pressure component is much greater than the friction component in propeller thrust, which is used to push the ship forward. While in high J (light loadings), the angle of attack is small and the pressure component decreases significantly, so the effect of prediction error of friction is obvious. As for the transition model, the results by the smaller I are better than that by the larger I, especially in high J. The results by the transition model with the larger I are close to that by the turbulence model. This is acceptable because when the turbulence intensity of fluid is strong, the laminar flow on the blade is easily turning to turbulence.

5. Results of propeller simulations

5.1. Pressure gradient on the blade surface

Fig. 17 shows the pressure gradient on a blade section (0.75R) of the propeller at two different advance coefficients. Fig. 17(a) and (b) shows the results of the propeller at a general advance coefficient ($J = 0.6$, $Re = 8.5 \cdot 10^5$), while Fig. 17(c) and (d) shows a special case when the propeller is very lightly loaded ($J = 1.4$, $Re = 9.6 \cdot 10^5$). For the general case, there is a long region of extremely strong F-P-G on the pressure side. A long region of extremely strong A-P-G exists on the suction side. From Fig. 17(b), the minimum pressure point is very close to the leading edge. Based on the results made in Section 3, the transition flow on the suction side can be estimated: the transition location is very close to the leading edge (it means that the laminar flow region on the suction side is very small). Considering that the F-P-G on the pressure side is much stronger than that shown in Fig. 9(a) and the results have been shown in Fig. 9(b), it can be estimated that the Re_T is a much great value. Therefore, the pressure side may be completely covered by pure laminar flow. For the special case, the pressure distribution is very different from that when $J = 0.6$ because the angle of attack of the flow to the blade section is negative. However, based on the pressure distributions, the transition flow can still be estimated. From Fig. 17(c) and (d), the transition location on the pressure side is close to the leading edge, while that on the suction side is close to the trailing edge. Besides, from Fig. 17, the pressure distributions predicted by the turbulence model and the transition model are basically the same.

5.2. Transition flow on the blade surface

The field function Turbulent Viscosity Ratio (*TVR*) is used for the study of the transition on the blade section. The *TVR* is defined as μ_t/μ, where μ is the natural molecular viscosity leading to shear stress in the fluid and μ_t is called the turbulent viscosity, which is defined by the formula $\mu_t = \rho kT$, where ρ is the density of the fluid, k is the turbulent kinetic energy, T is the turbulent time scale (Cd-Adapco, 2015). The turbulent viscosity is caused by the random fluctuating velocity, leading to additional shear stress (Reynolds stress). Thus, the ratio gives an indication about how strong the Reynolds stress compares to the molecular shear stress. In the laminar flow and laminar sub-layer of turbulent flow, there is
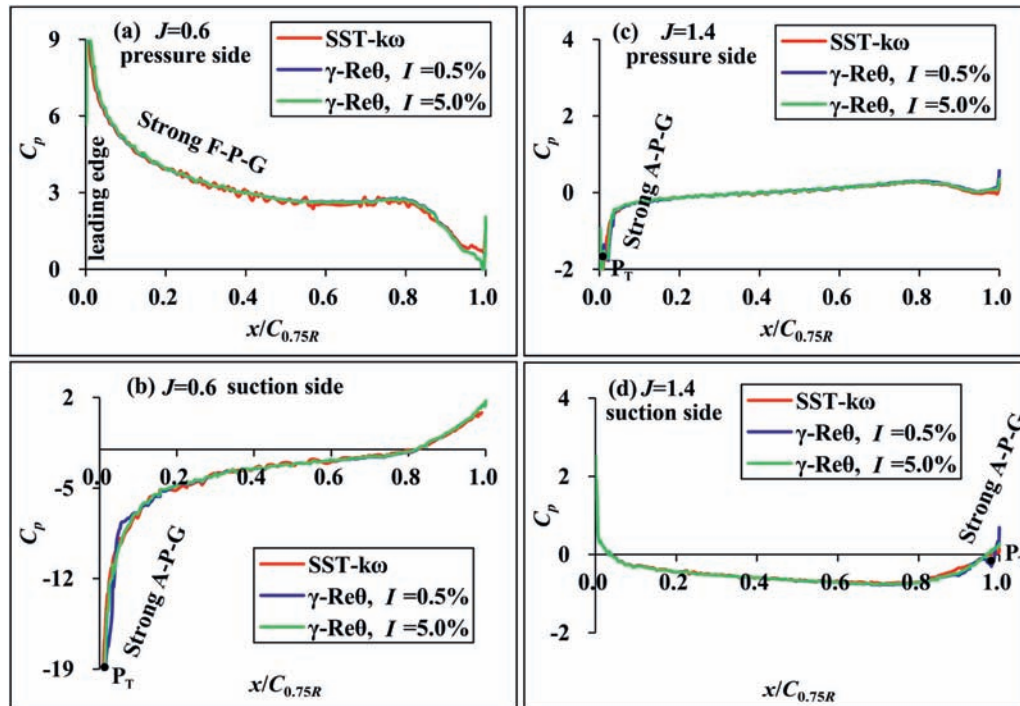
Fig. 17. Chord-wise distributions of pressure coefficients on the blade section (0.75R) of propeller VP1304, $n = 15$ Hz: (a) pressure side, $J = 0.6$, (b) suction side, $J = 0.6$, (c) pressure side, $J = 1.4$, (d) suction side, $J = 1.4$.

no turbulence and the ratio is zero. Otherwise, the ratio is a positive value.

Fig. 18 shows the transition flow on a blade section (0.75R) predicted by the turbulence model (SST-kω) and the transition model with two different I. First, let us focus on Fig. 18(b). Based on the numerical results predicted by the transition

model, the transition location on the suction side is very close to the leading edge, and the pressure side is completely covered by laminar flow. The results are consistent with our predictions in Section 5.1 based on the pressure gradient. Besides, the effect of turbulence intensity on the transition flow is negligible. However, from the results predicted by the
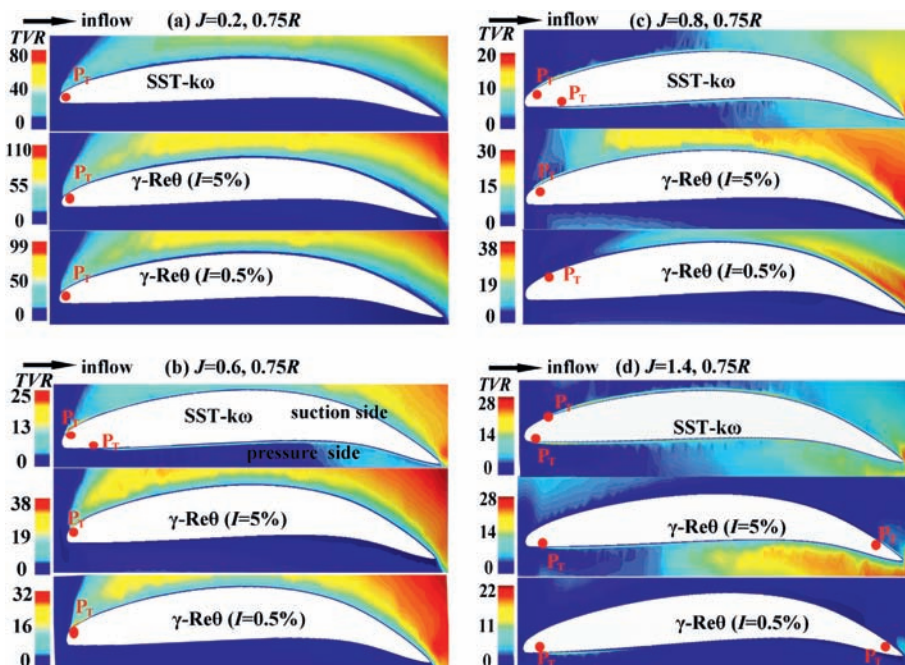

Fig. 18. Transition flows over the blade section (0.75R) of the model propeller VP1304 with different advance coefficients, $n = 15$ Hz: (a) $J = 0.2$, $Re = 8.3 \cdot 10^5$, (b) $J = 0.6$, $Re = 8.5 \cdot 10^5$, (c) $J = 0.8$, $Re = 8.7 \cdot 10^5$, (d) $J = 1.4$, $Re = 9.6 \cdot 10^5$.

turbulence model, the blade face is basically covered by turbulent flow, which is totally wrong. Second, the transition flows presented in Fig. 18(a) and (c) were discussed. Based on the results predicted by the transition model, the boundary layer flows of the blade section when $J = 0.2$ and 0.8 are similar with that when $J = 0.6$. This is because the pressure gradients on the blade section at these advance coefficients are similar. A closer look was paid to the effect of turbulence intensity on the transition location (Fig. 18(c)). It is clear that the transition locations (two different I values) are different but close to each other. As for the estimation of viscous force, such small difference is also negligible. From Fig. 18(d), it is clear that the transition location on the suction side is close to the trailing edge, and the transition location on the pressure side is close to the leading edge. The results are also consistent with our predictions in Section 5.1. However, the boundary layer flow over the blade section predicted by the turbulence model is basically turbulent.

Major conclusions of this section were summarized as follows:

➢ The transition location can be determined by the position of the minimum pressure point when there is strong A-P-G on the blade surface (mainly the blade back).
➢ If there is very strong F-P-G, then it is probable that the blade surface (mainly the blade face) is covered by pure laminar flow (applicable for the model propeller with general Reynolds numbers, less than $1.0 \cdot 10^6$).
➢ When there is strong A-P-G, the effect of turbulence intensity on the transition location is greatly reduced and can be negligible.

➢ The prediction of the transition flow over the model propeller blades by the turbulence model (SST-kω) is poor.

5.3. Friction distribution

Fig. 19 presents an alternative approach to study the transition flow on the propeller blade surface. Fig. 19(a) and (b) shows the results of the propeller blade section ($0.75R$) at a general advance coefficient ($J = 0.6$, $Re = 8.5 \cdot 10^5$), while Fig. 19(c) and (d) shows the results of a special case when the propeller is very lightly loaded ($J = 1.4$, $Re = 9.6 \cdot 10^5$). From Fig. 19(a), there is no sign of transition on the pressure side. From Fig. 19(b), the sign of transition on the suction side is very clear (the friction increases suddenly because the boundary layer flow turns from laminar flow to turbulent flow), and the location is close to the leading edge. From Fig. 19(c), the transition location on the pressure side is close to the leading edge, and the transition location on the suction side is close to the trailing edge (Fig. 19(d)). All these results are consistent with that shown in Fig. 18 and our predictions in Section 5.1. Besides, from Fig. 19(a) and (b), the effect of turbulence intensity on the friction forces is very small because there is strong F-P-G and A-P-G on the blade surface.

6. A simple method for estimating transition location

The study of this paper shows that the transition location is very close to the minimum pressure point when there is strong A-P-G. There are two methods to determine the position of the minimum pressure point accurately: experimental measurements
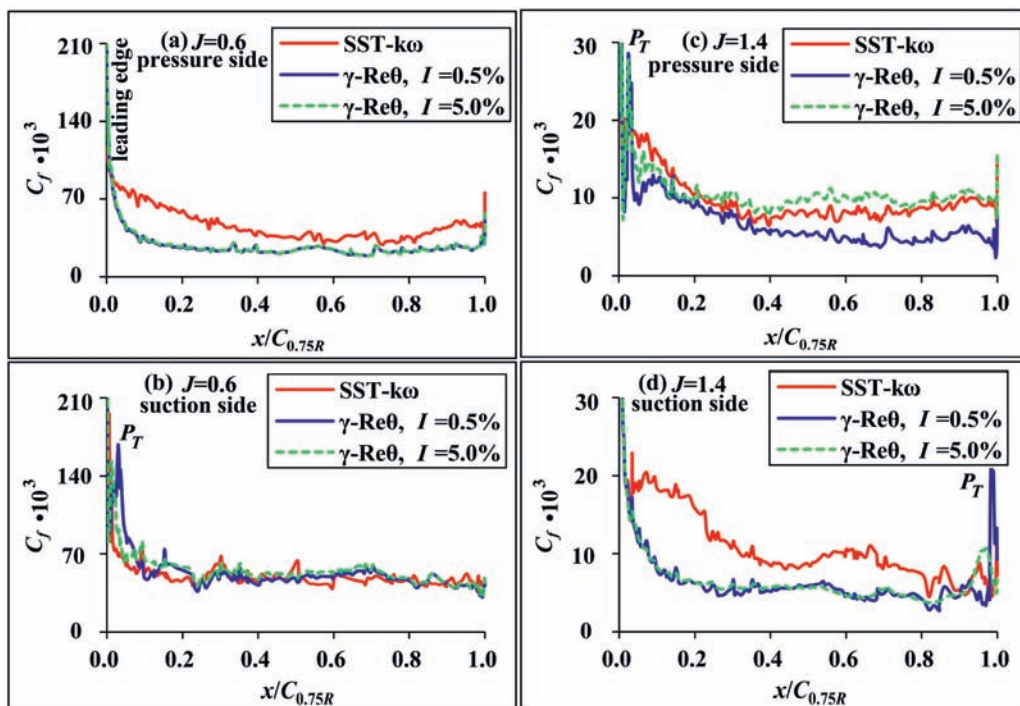

Fig. 19. Chord-wise distributions of friction coefficients on the blade section of propeller VP1304, $n = 15$ Hz: (a) pressure side, $J = 0.6$, (b) suction side, $J = 0.6$, (c) pressure side, $J = 1.4$, (d) suction side, $J = 1.4$.

and numerical methods. Considering the shortcomings of these two methods, this paper provides a simple method, which can be applied without any experimental data and any numerical results. The method is only based on the propeller geometry and the advance coefficient.

Fig. 20 shows a sketch for estimating the minimum pressure point on a blade section. In the figure, V_A is the advance velocity; V_n is the relative circumferential velocity; u_a and u_t are propeller induced axial and circumferential velocities, respectively; V_R is the resultant velocity; α_K is the angle of attack between the incoming flow (V_R) and the blade section. The induced velocities are unknown without measurements, but we do know that the induced velocities are much smaller than V_A and V_n, thus, the value of α_K can be approximated as α'_K. Then, the value of α'_K can be obtained using the following equation:

$$\alpha'_K = \theta - \beta \tag{1}$$

where θ and β are the pitch angle and the advance angle, respectively:

$$\theta = \arctan \frac{P}{2\pi r} \tag{2}$$

$$\beta = \arctan \frac{V_A}{2\pi nr} \tag{3}$$

where P is the pitch of the blade section and r is the radius of the blade section.

With the help of the following relations: $r = \eta R$, $D = 2R$, and $J = V_A/(nD)$, Eqs. (2) and (3) are rewritten as follows:

$$\theta = \arctan \frac{P}{n\pi D} \tag{4}$$

$$\beta = \arctan \frac{J}{n\pi} \tag{5}$$

where R is the radius of the propeller; η is a number between 0 and 1, which is determined by the position of the blade section. Therefore, α'_K of each section of the propeller in Eq. (1) is available, and the line marked as l_1 can be drawn based on this angle. The line marked as l_2 is parallel to l_1. Based on the basic knowledge of fluid mechanics, the point at which the l_2 is tangent to the suction side of the blade section is the minimum pressure point.
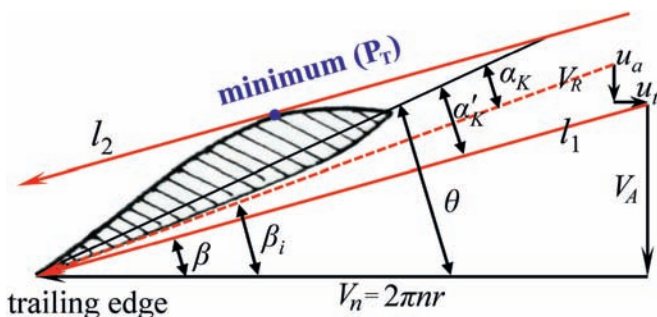

Fig. 20. Schematic diagram for estimating the position of the minimum pressure point to obtain the transition location.

7. Conclusions

In this paper, the transition flow on a model propeller blade surface was studied. The effects of Reynolds number, turbulence intensity and pressure gradient on the transition were investigated. Results show that the transition location is very close to the position of the minimum pressure point when there is strong adverse pressure gradient on the blade surface (mainly the blade back), and the Re_T increases significantly with the increase of the magnitude of favorable pressure gradient (considering the strong favorable pressure gradient on the blade face, it is very likely to be covered by pure laminar flow when Re is less than $1.0 \cdot 10^6$). Based on these conclusions, a very simple method was presented to estimate the transition location on the blade surface. The method can be applied without any experimental data and any numerical results and is based on the propeller geometry and the advance coefficient.

The presented work focused on figuring out the method to estimate the transition locations on propeller blade surface. More detailed information about the mathematical methods for calculating friction coefficient of the whole blade and studying scale effects can be found in Streckwall et al. (2013).

Results also show that the transition Reynolds number on the blade surface varies strongly with the inflow Reynolds number, turbulence intensity and pressure gradient. Considering that the Reynolds number varies strongly along the radius from the blade root to the blade tip, using only two different transition Reynolds numbers for both sides of the blade to distinguish the laminar and turbulent region on the blade surface by the strip method may have considerable errors.

Results show that the effect of turbulence intensity on the transition is greatly reduced when there is strong pressure gradient. Therefore, if numerical methods are applied for studying the transition flow on marine propellers without knowing the turbulence intensity because the turbulence intensity is usually not measured in experiments, then, the propeller with heavily-loaded conditions should be selected for the study.

Results show that the transition flow and friction distributions on model propeller blade surface cannot be well predicted by SST-kω model, but the pressure distributions on the blade surface are accurately predicted by the turbulence model.

Acknowledgments

References

Barkmann, U., 2011. Potsdam Propeller Test Case (PPTC) − Open Water Tests with the Model Propeller VP1304. Report 3752. Schiffbau-Ver-suchsanstalt Potsdam.

Bhattacharyya, A., Krasilnikov, V., Steen, S., 2015. Scale Effects on a 4-Bladed Propeller Operating in Ducts of Different Design in Open Water. In: Fourth International Symposium on Marine Propulsors, Austin, Texas.

Bhattacharyya, A., Krasilnikov, V., Steen, S., 2016a. Scale effects on open water characteristics of a controllable pitch propeller working within different duct designs. Ocean Eng. 112, 226−242.

Bhattacharyya, A., Krasilnikov, V., Steen, S., 2016b. A CFD-based scaling approach for ducted propellers. Ocean Eng. 123, 116—130.

Cd-Adapco, 2015. Star-CCM+, User and Theory Manual, version 7.04.011.

Chaput, E., 1997. Application-Oriented Synthesis of Work Presented in Chapter II (Chapter 3). In: Notes on Numerical Fluid Mechanics, vol. 58, pp. 327—346.

Helma, S., 2015. A scaling procedure for modern propeller designs. Ocean Eng. 120, 165—174.

ITTC, 1978. ITTC Performance Prediction Method. Recommended Procedures and Guidelines, 7.5—02 — 03—01.4.

ITTC, 2014. In: Proceedings of the 27th ITTC Conference, August 31, Copenhagen, Denmark.

Malan, P., Suluksna, K., Juntasaro, E., 2009. Calibrating the γ-Reθ transition model for commercial CFD. In: 47th AIAA Aerospace Sciences Meeting, 5—8.

Mach, K.P., 2011. Potsdam Propeller Test Case (PPTC) — LDV Velocity Measurements with the Model Propeller VP1304. Report 3754. Schiffbau-Versuchsanstalt Potsdam.

Meyne, K., 1968. Experimentelle und theoretische Betrachtungen zum Maß-stabseffekt bei Modellpropeller-Untersuchungen. In: Schiffstechnik, vol. 15.

Menter, F.R., Langtry, R.B., Likki, S.R., Suzen, Y.B., Huang, P.G., Völker, S., 2006. A correlation-based transition model using local variables—part I: model formulation. J. Turbomach. 128 (3), 57—67.

Müller, S.B., Abdel-Maksoud, M., Hilbert, G., 2009. Scale Effects on Propellers for Large Container Vessels. In: In the first International Symposium on Marine Propulsors, Trondheim, Norway.

Müller, S.B., 2013. Numerische Untersuchung der Maßstabseffekte an Schiffspropellern (Ph.D. thesis). Abteilung Maschinenbau, Universität Duisburg-Essen, Deutschland.

Praefke, E., 1994. Multi-Component Propulsors for Merchant Ships — Design Considerations and Model Test Results. In: SNAME Symposium "Propeller/Shafting '94", Sept. 20—21, Virginia, USA.

Sánchez-Caja, A., González-Adalid, J., Pérez-Sobrino, M., Sipilä, T., 2014. Scale effects on tip loaded propeller performance using a RANSE solver. Ocean Eng. 88 (5), 607—617.

Schubauer, G.B., Klebanoff, P.S., 1955. Contributions on the Mechanics of Boundary Layer Transition. NACA Technical Note.

Streckwall, H., Greitsch, L., Müller, J., Scharf, M., Bugalski, T., 2013. Development of a strip method proposed to serve as a new standard for propeller performance scaling. Ship Technol. Res. 60 (2), 58—60.